JGR Solid Earth

Key Points:
- The new crustal model beneath the Okmok Caldera with the 3D distributions of *Vp*, *Vs* and *Vp/Vs* ratio reveals the geometry of magma sources
- Below 10 km depth, an anomaly of high *Vp/Vs* ratio indicates the location of the main magma conduit that fed the long-term formation of Okmok
- At shallow depths, seismic anomalies reveal several magma sources that fed eruptions along the inner perimeter of the caldera

Correspondence to:
I. Koulakov,
KoulakovIY@ipgg.sbras.ru

Author Contributions:
Conceptualization: Ronni Grapenthin, Pavel Izbekov, Jessica F. Larsen, Nassir Al Arifi, Saleh Ismail Qaysi
Data curation: Nassir Al Arifi
Formal analysis: Ekaterina Kasatkina, Saleh Ismail Qaysi
Investigation: Ekaterina Kasatkina, Ivan Koulakov, Ronni Grapenthin, Pavel Izbekov, Nassir Al Arifi, Saleh Ismail Qaysi
Methodology: Ivan Koulakov
Resources: Pavel Izbekov, Saleh Ismail Qaysi
Software: Ivan Koulakov
Supervision: Ivan Koulakov

Multiple Magma Sources Beneath the Okmok Caldera as Inferred From Local Earthquake Tomography

Ekaterina Kasatkina[1] , Ivan Koulakov[1,2,3] , Ronni Grapenthin[4] , Pavel Izbekov[4], Jessica F. Larsen[4], Nassir Al Arifi[5] , and Saleh Ismail Qaysi[5]

[1]Trofimuk Institute of Petroleum Geology and Geophysics SB RAS, Novosibirsk, Russia, [2]Institute of the Earth's Crust SB RAS, Irkutsk, Russia, [3]Institute of Volcanology and Seismology FEB RAS, Petropavlovsk-Kamchatsky, Russia, [4]Geophysical Institute, University of Alaska Fairbanks, Fairbanks, AK, USA, [5]Chair of Natural Hazards and Mineral Resources, Geology and Geophysics Department, King Saud University, Riyadh, Saudi Arabia

Abstract Okmok volcano located on the northeastern part of the Umnak Island is one of the most active volcanoes in the Aleutian Arc. It was initially built as a large shield volcano, but 12,000 and 2,050 years ago, it experienced two caldera-forming eruptions that destroyed the central part of the volcano. The post-caldera eruptions have occurred mostly along the inner perimeter of the caldera from cinder and tuff cones. Here, we use the local earthquake data of the Alaska Volcano Observatory (AVO) in the time period from 2003 to 2017 to build a model with the 3D distributions of the *P* and *S* wave velocities and *Vp/Vs* ratio. At depths of more than 10 km, we observe a vertically aligned anomaly of high *Vp/Vs* ratio interpreted as a long-lived conduit likely responsible for the volcano evolution since its origin. Above this conduit, we reveal a large anomaly of high *Vp/Vs* ratio representing the main magma reservoir that is connected with several shallow anomalies located below the centers of recent eruptions in the caldera. One of such anomalies represents a large shallow reservoir below the Cone A, which was the source of most of Okmok's historical eruptions. The most recent eruption occurred in 2008 and was fed by a magma diapir that was initially formed in the central magma reservoir and then slowly ascended through a ductile silica rich layer at depths from 6 to 2 km. This interpretation is consistent with the petrology studies and modeling of ground deformations.

Plain Language Summary Okmok is one of the most active volcanoes of the Aleutian Arc. Initially it was formed as an isometrical shield volcano, which was later destroyed by two caldera-forming eruptions. The post-caldera activity mostly occurred at several cones distributed along the inner perimeter of the caldera. The latest eruption with the explosivity index of VEI 4 took place in 2008. This eruption, which produced a new large cone Ahmanilix in the northeastern part of the caldera, was significantly different in composition and eruption style compared to other intra-caldera eruptions. We present a new seismic tomography model, which was constructed based on the arrival times of the *P* and *S* waves from local seismicity. Below 10 km depth, we observe an anomaly of high *Vp/Vs* ratio, which may represent a steady magma conduit that is responsible for the long-term formation of the entire Okmok volcanic complex. In the upper crust, the model reveals a series of separate local magma sources beneath volcanic centers where historical eruptions took place. The 2008 eruption was fed by a magma diapir that was initially formed in the deep conduit and then slowly ascended through a ductile layer at depths from 6 to 2 km.

1. Introduction

Okmok is one of the most active volcanoes of the Aleutian Arc. Initially, it was formed as a large circular shield volcano with a diameter of ~30 km that occupies the northeastern half of the dumbbell-shaped Umnak Island. According to K-Ar dating, volcanism in northeastern Umnak Island began approximately 1.7–2.1 Ma (Bingham & Stone, 1972), eventually localizing to the modern Okmok shield volcano. Thus, long-term magmatic activity has occurred in this region for millions years. The central part of this volcano was destroyed by at least two ignimbrite-forming eruptions 12,000 and 2,050 years ago (Larsen et al., 2007) that created two over-lapped well-exposed circular calderas that are each ~10 km across (Figure 1). The amount of material in dense rock equivalent for these two eruptions was estimated as 30 and 15 km³, respectively (Burgisser, 2005; Larsen et al., 2007). These eruptions had an important impact on the climate that was felt globally. There is evidence that the latter eruption affected people in Europe and caused serious historical weather perturbations (McConnell et al., 2020). Atypical for caldera-forming eruptions, the products of these two eruptions contained very little

Validation: Ekaterina Kasatkina, Jessica F. Larsen, Nassir Al Arifi

Visualization: Ekaterina Kasatkina, Ivan Koulakov

Writing – original draft: Ekaterina Kasatkina, Ivan Koulakov

Writing – review & editing: Ivan Koulakov, Ronni Grapenthin, Jessica F. Larsen, Nassir Al Arifi, Saleh Ismail Qaysi

amount of rhyolite and dacite magmas, which were ejected at the initial stages, but then were replaced by a larger amount of andesite and basaltic andesite (Larsen et al., 2007).

The post-caldera eruption activity mostly occurred along the inner perimeter of the caldera through a series of vents some of which created well-expressed cinder and tuff cones (Figure 1). The compositions of these eruptions range from basalt to andesite (Larsen et al., 2013). The oldest flows were composed of pillow lavas, which indicated that the caldera was initially filled by a deep lake (Larsen et al., 2007). Nowadays, in the caldera, there are several shallow lakes that are abruptly changing their configurations during eruptions.

At least 17 historical explosive and effusive eruptions have been recorded on Okmok since the beginning of the nineteenth century (Larsen et al., 2015). The majority of these eruptions occurred from Cone A in the southwestern part of the caldera (Figure 1). In the twentieth century, the well-documented eruptions with basaltic-andesite lava flows and moderate ash falls occurred in 1945, 1958 and 1997 exclusively from vent A (e.g., Larsen et al., 2015; Miller et al., 1998).

The latest eruption, with a high explosivity index of VEI 4, took place in July–August 2008 and was similar to the 1817 eruption in style and strength. It occurred in the northeastern part of the caldera close to the Cone D and produced a new large cone called Ahmanilix. This eruption was classified as explosive phreatomagmatic eruption with a large amount of steam, ash and tephra ejected. According to the geochemical analyses by Larsen et al (2013), the eruption products in this part of caldera are distinctively different from those in the southwestern part around Cone A; namely they have higher SiO_2 content. A specific feature of the 2008 eruption is that it did not produce any lava flows (Larsen et al., 2015). The eruption of 2008 was not preceded by any significant seismic precursors. For 10 days prior to the eruption, only 11 locatable earthquakes with the magnitudes of more than 1 were recorded. An active seismogenic process started only 5 hours before the eruption onset (Larsen et al., 2009).

Okmok's dynamic and near-continuous deformation during and in between eruptions made it the subject of many studies using GPS, InSAR, or both to constrain its subsurface magma system structure and its evolution. The 1997 and 2008 eruptions caused meter-scale deflation of the caldera center (e.g., Freymueller & Kaufman, 2010; Mann et al., 2002), while inter-eruptive deformation is characterized by discrete inflation pulses modulated onto steady background inflation of several centimeters per year (e.g., Qu et al., 2015; Xue et al., 2020). Inversions of InSAR data (e.g., Lu & Dzurisin, 2014; Lu et al., 2000; Mann et al., 2002; Qu et al., 2015), GPS data (e.g., Fournier et al., 2009; Freymueller & Kaufman, 2010) or joint inversions of both (e.g., Biggs et al., 2010; Xue et al., 2020) generally yield a spherical magma reservoir near the center of the caldera between 2 and 5 km depth, with most results placing the source between 2 and 3.5 km. Xue et al. (2020) suggested that in addition to this spherical source a shallow sill at about 0.9 km is necessary to explain the post-2008 geodetic observations. They also count five inflation pulses for 11 years since the 2008 eruption that emerge rapidly and slow down following an exponential decay. Walwer et al. (2019) explained the origin of these short-term inflation pulses by hydraulic interaction between two shallow magma chambers.

Another group of studies examined structure and dynamics of magma sources beneath Okmok based on the analysis of seismic data, which were continuously recorded by a network of permanent telemetric seismic stations operated since 2003 (Dixon et al., 2017). The temporal and spatial distributions of volcano-tectonic events during the eruption in 2008 were investigated by Johnson et al. (2010), who also provided estimates for seismic anisotropy based on the shear wave splitting technique. Moment tensors of these events were determined by Pesicek et al. (2012). Haney (2010) investigated the very long-period seismicity, which was the indicator of magma dynamics in the conduit and therefore was considered as one of the eruption precursors.

In the context of this research, it is important to mention the previous seismic tomography studies of the Okmok area. Ambient noise tomography was used by Masterlark et al. (2010) to build the 3D distribution of the *S*-wave velocity down to 7 km depth. They identified a low-velocity anomaly below the caldera at depths down to ∼2 km, which was interpreted as deposits of non-consolidated rocks accumulated after the latest caldera-forming eruptions. Another anomaly was observed at depths of 3–5 km below the caldera and was associated with the presence of the shallow magma reservoir. Later this model was used together with data on ground deformations to validate the numerical model of magma source dynamics (Masterlark et al., 2012). However, it should be noted that this model was constructed on the basis of only 12 stations, which provided a limited number of inter-station paths and could not enable high lateral resolution of the resulting velocity distribution. Furthermore, nine of these
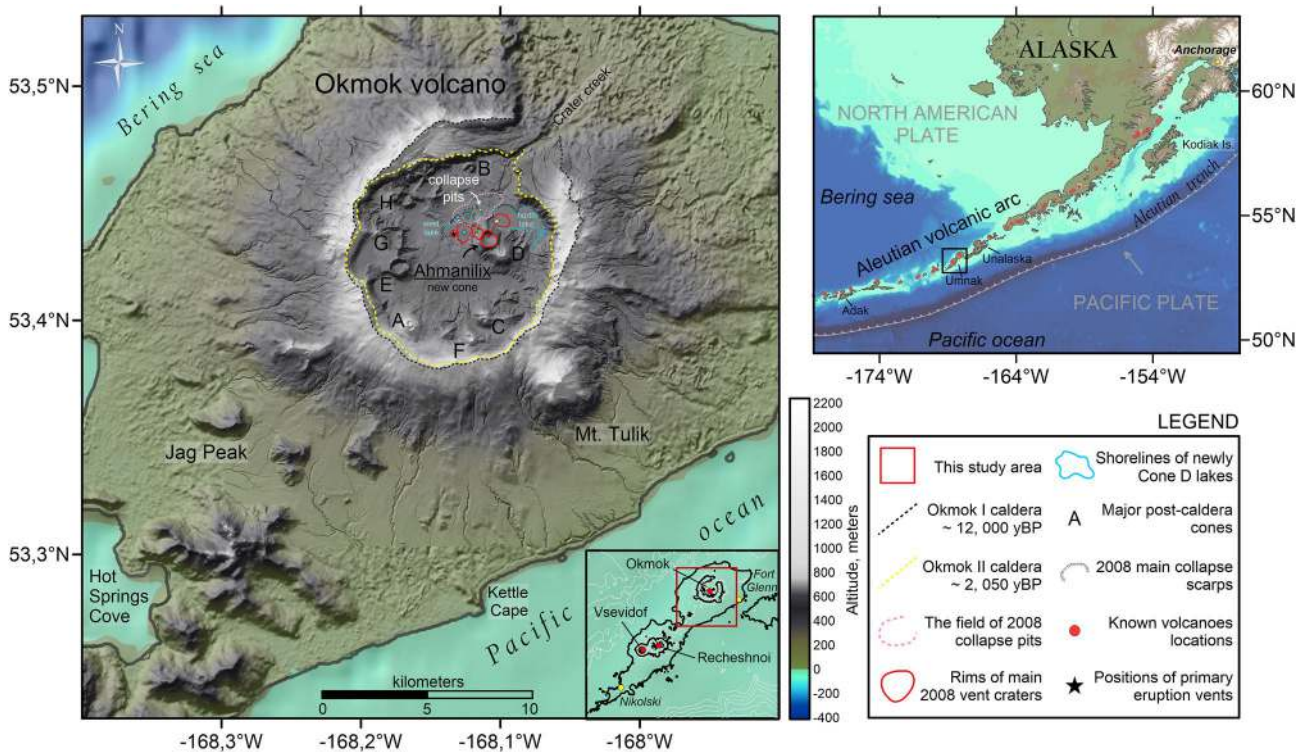
Figure 1. Shaded-relief map of the Okmok volcano (Umnak Island, Alaska) and its location within the Aleutian volcanic arc. Main eruptive features in the caldera shown after Larsen et al. (2015) and represent the recent 2008 eruption formations—new tephra cone with additional vents, area of collapsing pits and two renewed Cone D lakes. Post-caldera cones marked by letters after Byers (1959). Base map topography and bathymetry data was loaded from www.marine-geo.org (GRMT data, Ryan et al., 2009); central part of the map (including caldera) have been constructed with detailed DEM data from Schaefer et al. (2012). See features descriptions in the legend.

stations were equipped by single-component short period sensors (1 Hz), which strongly limited the depth coverage of the surface wave tomography.

Another tomography model by Ohlendorf et al. (2014) was constructed based on the local earthquake tomography using generally the same principle and data type as in our work. They reported both the models of the *P* and *S*-wave velocities, as well as the distribution of the *P*-wave attenuation; however, the authors admitted that their *S*-wave model was based on too sparse data coverage and therefore was not robust. Similarly as in the model by Masterlark et al. (2010), the body wave tomography revealed low *P*-wave velocity beneath the caldera; however, the *S*-wave velocity was unexpectedly high in the same locations. Note also, that in this model, the resolution suffered from large grid spacing (2.5 × 4 km laterally and from 1 to 6 km in the vertical direction) making the results strongly grid-dependent. Furthermore, the authors did not present the distribution of the *Vp/Vs* ratio, which appeared to be the key parameter to identify magma sources beneath active volcanoes.

In this study, we construct a new seismic velocity model based on a considerably enlarged data set and using another tomography code LOTOS (Koulakov, 2009a), which previously demonstrated its efficiency for studying different volcanic systems in the world (Bushenkova et al., 2019; Kasatkina et al., 2014; Koulakov et al., 2013). Here, we will pay special attention to showing the distributions of the *Vp/Vs* ratio, which is presumed the most sensitive seismic attribute to the presence of partially molten and fluid saturated magma. In this study, we will present several synthetic tests showing the resolution limitations of our model. Therefore, the results presented in this work give important new information on the magma system structure beneath Okmok compared to the previous studies and therefore brings an important contribution to understanding the processes leading to initiation of eruptions.
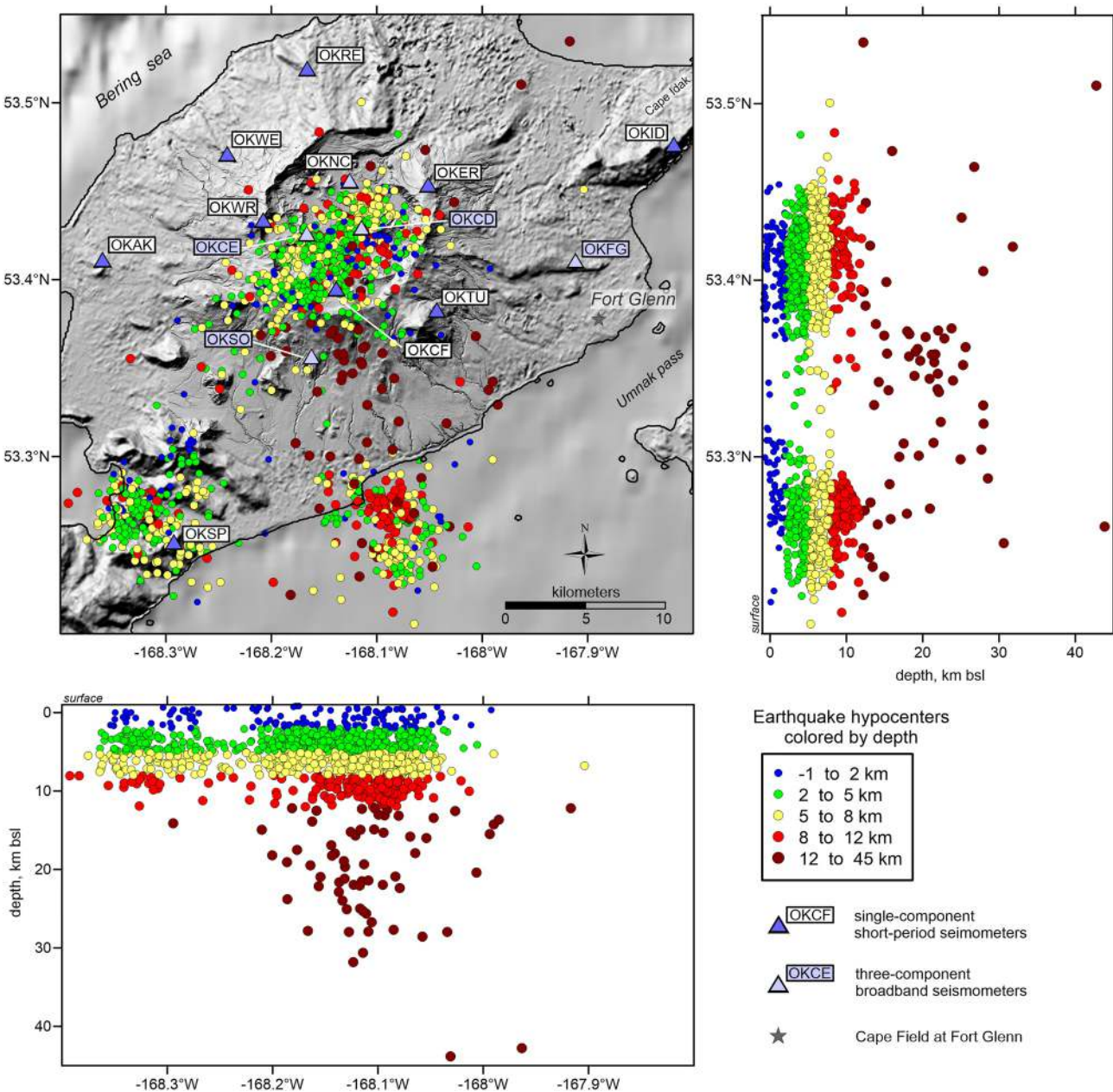
Figure 2. Seismic network on the Okmok volcano and spatial seismicity distribution used for tomographic inversion in this study. Seismic events (2003–2017) are shown by dots colored by focal depth. Purple and lilac triangles depict two types of seismic instruments with its ID's. Gray star indicate Ranch house at Fort Glenn Cape field.

2. Data and Algorithms

In this work, we use the catalog data from 2003 to 2017, which includes the arrival times of the *P* and *S* waves from local seismicity recorded by 13 permanent telemetric stations located around Okmok and operated by the Alaska Volcano Observatory (AVO) (Dixon et al., 2017). Of these stations, four are equipped with broadband seismometers Guralp CMG-6T; the remaining nine consist of short-period (1 Hz) single-component sensors L-4 (Figure 2). However, for determination of arrival times from the local seismicity, the frequency ranges of both types of seismometers are equally suitable. The initial catalog includes 4,174 events and the corresponding arrival times of 19,249 *P* and 14,278 *S* waves (on average 8.03 picks per event). To select data for the tomography inversion, we applied several criteria: (a) the number of picks per event should be equal or larger 8; (b) the horizontal

distance from an event to the nearest station should be less than 20 km; (c) the time residuals after the source location in the starting 1D model should be smaller than 0.5 and 0.85 s for the *P* and *S* waves respectively. Note that the later criterion caused the rejection of approximately 9% and 5% of the *P* and *S* picks, respectively, which indicate high quality of the initial AVO catalog having a relatively small number of misinterpreted phases. After the selection, the final data set used for tomography included 2869 events with the corresponding 17,040 *P*- and 12,145 *S*-picks (on average 10.17 picks per event).

We note that the small number of horizontal component stations necessitated using *S* wave picks made on vertical component stations. There might be a concern that *S-P* conversions, which would arrive earlier than the direct *S* wave, can be misinterpreted as *S* and possibly result in shallower hypocenters and/or faster *S* wave velocities. However, if at some stations, the arrival times of the *S* phases were wrong, they would be possibly considered as outliers and would be rejected at the stage of data selection. At the same time, the number of the *S*-phases that did not pass the threshold criterion of 0.85 s was only 643 of 12,788 (5.02%), which is relatively small. If some of the misinterpreted phases remained in the data set, it would be nearly impossible to find locations of sources that enabled small residuals at all stations. Actually, as will be shown later, the inversion provided a significant variance reduction and small average residuals, which may indicate a minor amount of erroneous phases in the data set. For all these reasons, we claim that in our case a significant bias of event locations due to the misinterpretation of phases is unlikely.

The distributions of the events and seismic stations are shown in map view and in vertical projections in Figure 2. Further information on the event distributions after locations in the final 3D velocity model will be presented in cross-sections with the main tomography results.

These data were processed using the passive-source tomography algorithm LOTOS (Koulakov, 2009a). As the input, the algorithm uses the arrival times of the *P* and *S* waves and it starts with the absolute locations of sources using the grid-search method and a simplified algorithm for travel time calculations along straight lines. Then the relocation of the sources is performed in an iteratively updated 3D velocity model with the use of a more sophisticated ray tracing algorithm based on a bending technique (Um & Thurber, 1987). In this case, the rays are calculated between the stations and events at the actual elevations/depths.

The velocity model is parameterized with a set of nodes distributed in 3D space. In map view, the nodes are installed regularly with a spacing of 1 km. In the vertical direction, the nodes are installed downward from the topography surface. The node spacing is inversely dependent on the ray coverage in the range from 0.5 to 3 km. In areas without rays, no nodes are installed. To reduce the effect of parameterization on the results, we performed the inversions in four grids with different basic orientations along the azimuths of 0, 22, 45 and 66°, and then averaged the results. Examples of grid construction according to the ray density for the *P*- and *S*-wave data in different depth intervals are shown in Figure 3. It can be seen that the distributions of the *P* and *S* data and grids are very similar, which enables similar resolution for these two types of data. In turn, this provides the robust recovery of the *Vp/Vs* ratio.

The inversion of the matrix was performed simultaneously for 3D *P* and *S* wave velocity anomalies (*dVp* and *dVs*) and source relocation parameters (coordinate shifts, *dx, dy, dz*, and origin time correction, *dt*). The inversion was performed using the Least Square algorithm with QR factorization (LSQR) (Nolet, 1987; Paige & Saunders, 1982). To regularize the stability of the resulting velocity models, we used the least squares damping to tune the amplitudes of anomalies and flattening to control the velocity gradient at the parameterization nodes. In our case, the values of the amplitude damping for the *P* and *S*-wave models were 0.5 and 1, respectively; the corresponding flattening coefficients were 0.7 and 1.5. These regularization parameters were identified based on the results of synthetic modeling, which will be presented below.

The iterative cycle included the steps of source locations in the updated 3D velocity model, matrix calculation, inversions for four different grids and calculation of the new averaged 3D model in a regular grid. In total, we performed five iteration cycles, which was an appropriate compromise between the model stability and calculation speed. Note also that the tomography inversion provides the 3D distributions of the *P* and *S* wave velocity anomalies. The distribution of the *Vp/Vs* ratio is calculated by simple division of the resulting absolute *Vp* and *Vs*. The adequacy of this approach was tested by a series of synthetic tests, which will be presented in the next section.

As a starting model, we used the 1D velocity distribution, which was defined at several depth levels and linearly interpolated. For the first run of the tomography procedure, we took a model from Akutan island (Koulakov
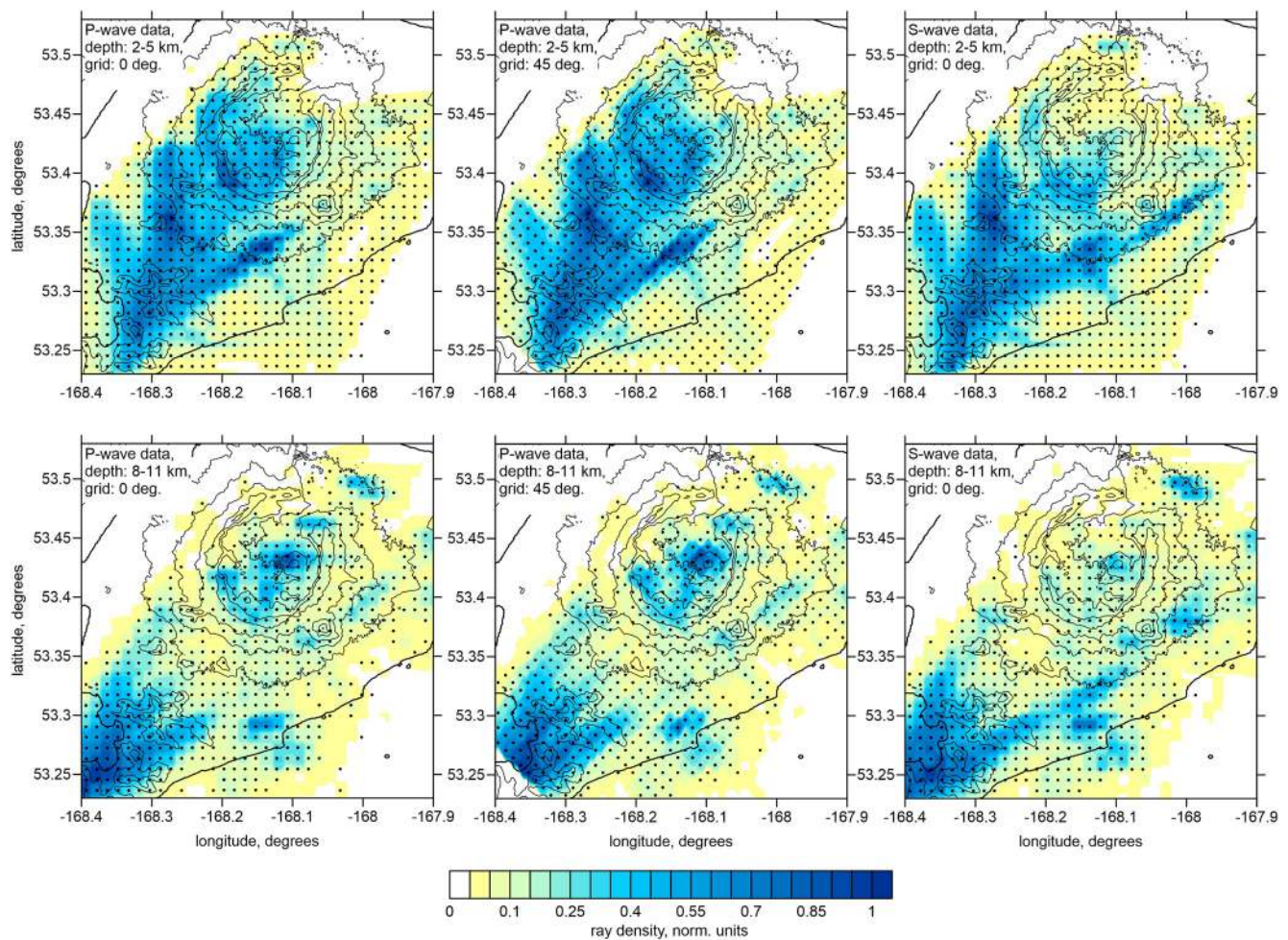
Figure 3. Examples of grid construction according to the ray density. The dots depict the nodes in the indicated depth intervals; background is the normalized ray density. First column is the grid with the orientation of 0 for the *P*-wave data; second column is the grid with the orientation of 45° for the *P*-wave data and third column is the grid with the orientation of 0° for the *S*-wave data.

et al., 2021), which presumably has similar structure. After completing the calculations, we calculated average *P*-wave velocities in horizontal levels and used them as a new starting velocity model. The *S*-wave velocities in the starting model were always calculated according to the constant *Vp/Vs* ratio. After several iterations, we have obtained a model for which a prompt balance between the positive and negative anomalies was achieved. The values of the *P*-wave velocity in this model are presented in Table 1. In this model, the *Vp/Vs* ratio was equal to 1.75.

Table 1

P-Wave Velocities in the Starting Model Used to Calculate the Main Results

Depth, km	Vp, km/s
1	4.53
4	4.73
7	4.88
10	5.11
30	7.8

Note. The *S*-wave velocity was calculated according to the constant *Vp/Vs* ratio equal to 1.75.

3. Synthetic Tests

Before presenting the main velocity models, we show the results of several synthetic tests demonstrating resolution limitations of the tomography results. We perform synthetic modeling to simulate the conditions of the experimental data processing as closely as possible. The synthetic data are produced for the same source-receiver pairs, as in the experimental data set. The sources in the synthetic model are identical to the event locations calculated in the main tomography model based on the experimental data. The synthetic travel times are calculated in the predefined 3D synthetic velocity model with the use of the bending ray tracing algorithms. The travel times are then perturbed by random noise with average deviations in the L1 norm
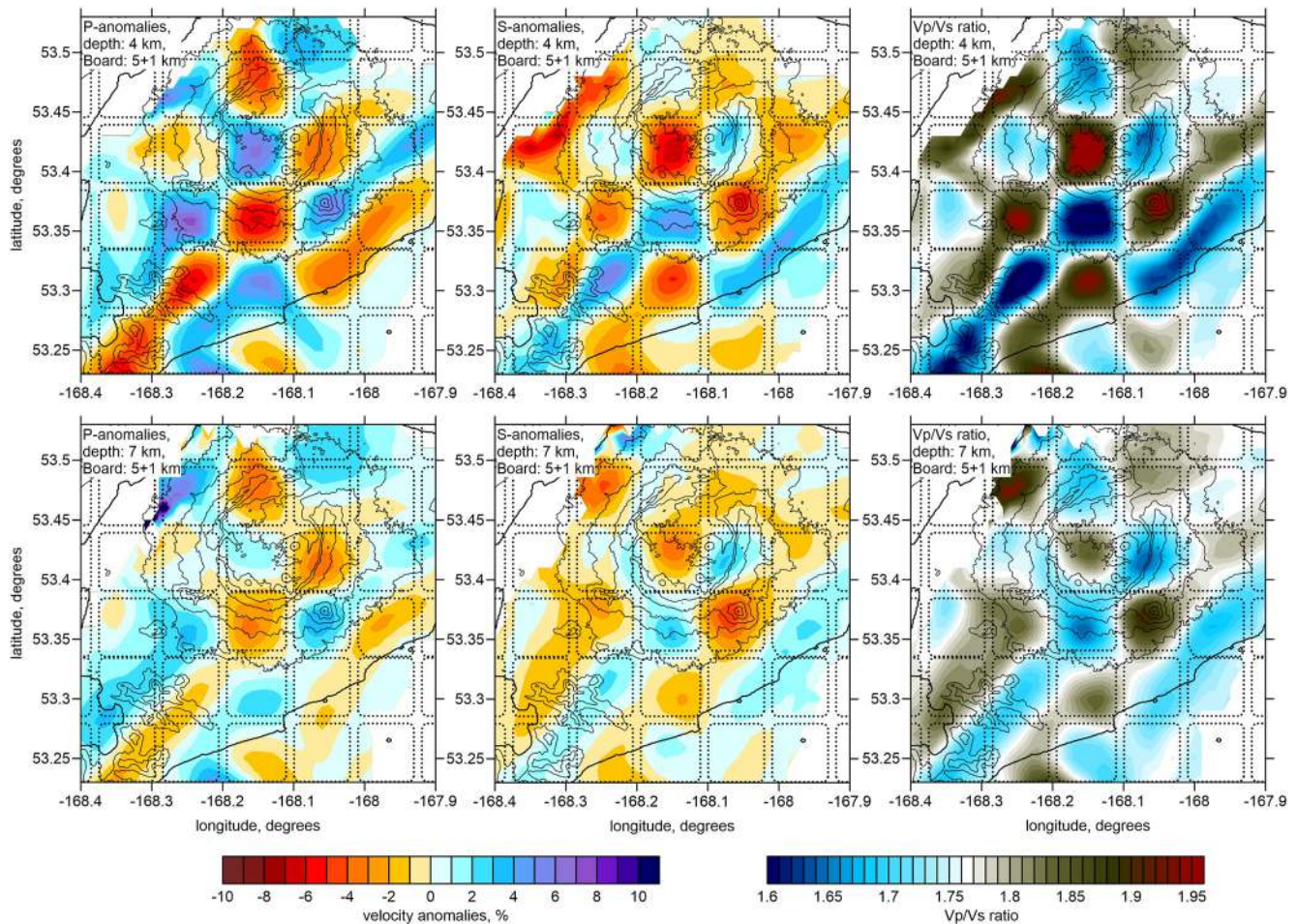
Figure 4. Results of the checkerboard test for determining horizontal resolution. Results of recovery are presented for *P*-, *S*-, and *Vp/Vs* models at 4 and 7 km depth levels. Initial configuration of synthetic 5-km-side anomalies with 1 km intervals is highlighted with the dotted lines. The thin black lines shows topography contours with 200 m intervals.

equal to 0.03 and 0.05 s for the *P* and *S* wave data, respectively. Then we "forget" any information about source coordinates and origin times and start the recovery using the same workflow as in the case of experimental data inversion, including the initial step of absolute source locations. All the controlling parameters in the synthetic modeling remain the same as in the case of computing the main model. In all tests, we started the recovery with the same 1D reference model having the constant *Vp/Vs* ratio equal to 1.75.

Here, we separately analyze the horizontal and vertical resolution based on the same sections as used for presenting the main results. In the first test presented in Figure 4, we define the horizontal checkerboard model with alternated positive and negative anomalies of ±8% having the size of 5 km and separated by 1 km intervals. For the *P* and *S* wave models, we defined the opposite signs of the anomalies to enable high contrasts of the *Vp/Vs* ratio variations. In the vertical direction, the anomalies remain unchanged at all depths. In the resulting horizontal sections in Figure 4, we can see that the anomalies are correctly recovered at all depths down to at least 7 km, although, in the deeper sections, the amplitudes of anomalies become weaker, which is explained by considerably smaller amounts of data.

In the next series of tests, we explore the vertical resolution of the models, which is usually poorer than the horizontal resolution due to the trade-off between velocity and source parameters (especially of focal depths). In Figure 5, we present three synthetic models separately defined along three vertical sections used for presenting the main results. Along the sections, we defined alternated anomalies with the amplitudes of ±8% having the sizes of 5 by 6 km. In the horizontal direction, they are separated by a 1 km interval. In the vertical direction, the interval is 2 km. The change of the anomaly sign occurs at the depth internals of 2–4 km and 10–12 km. As in
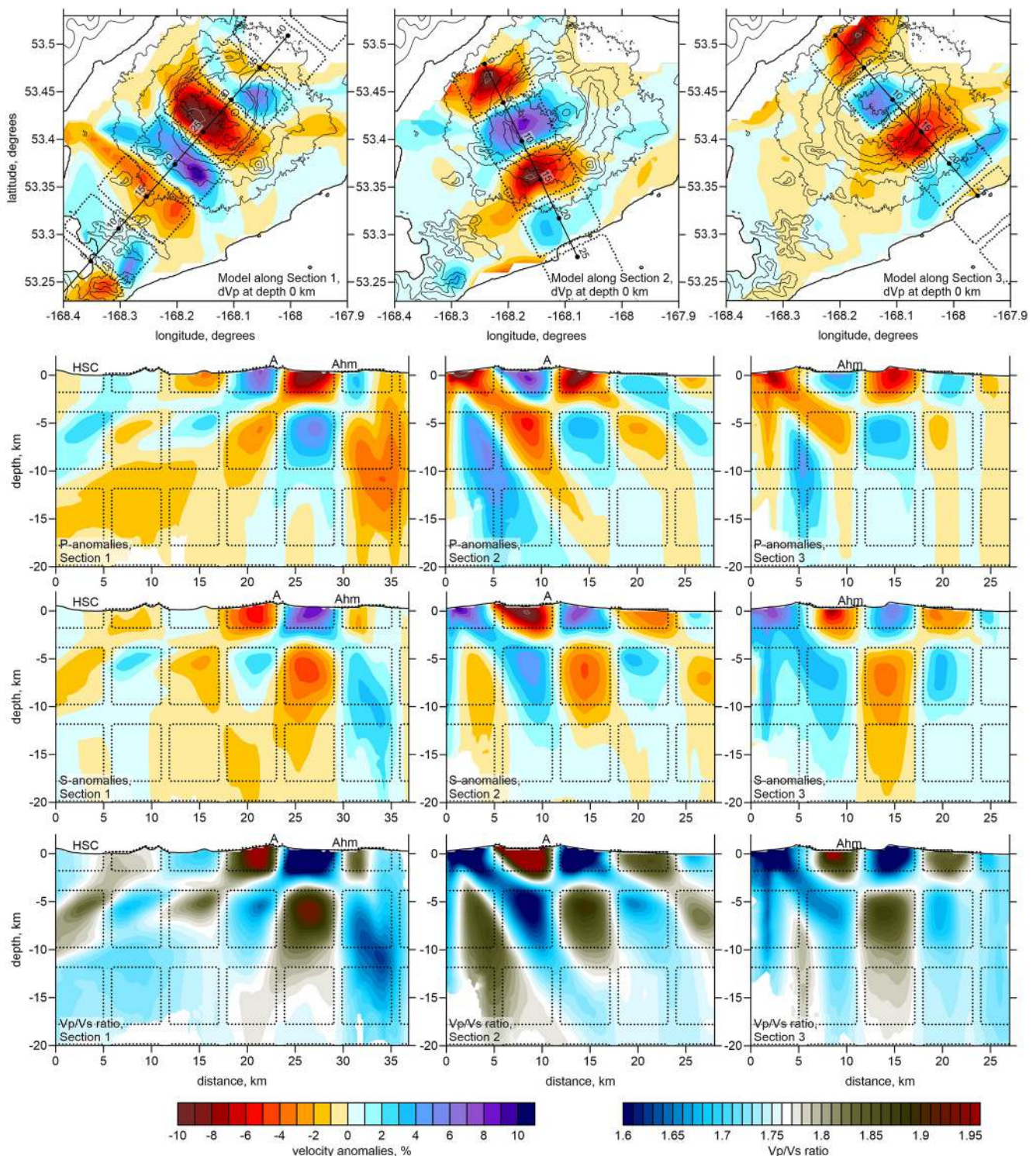
Figure 5. Results of three checkerboard tests for checking the vertical resolution in which the synthetic models were defined along three vertical sections. The recovery results are presented for the *Vp* and *Vs* anomalies and *Vp/Vs* ratio. The shapes of the synthetic anomalies are highlighted with the dotted lines. Upper row shows the configuration of the synthetic anomalies and recovery results for *dVp* for three models in map view at 0 km depth. Abbreviations: HSC—Hot Spring Cove; A—Cone A; Ahm—Ahmanilix Cone.
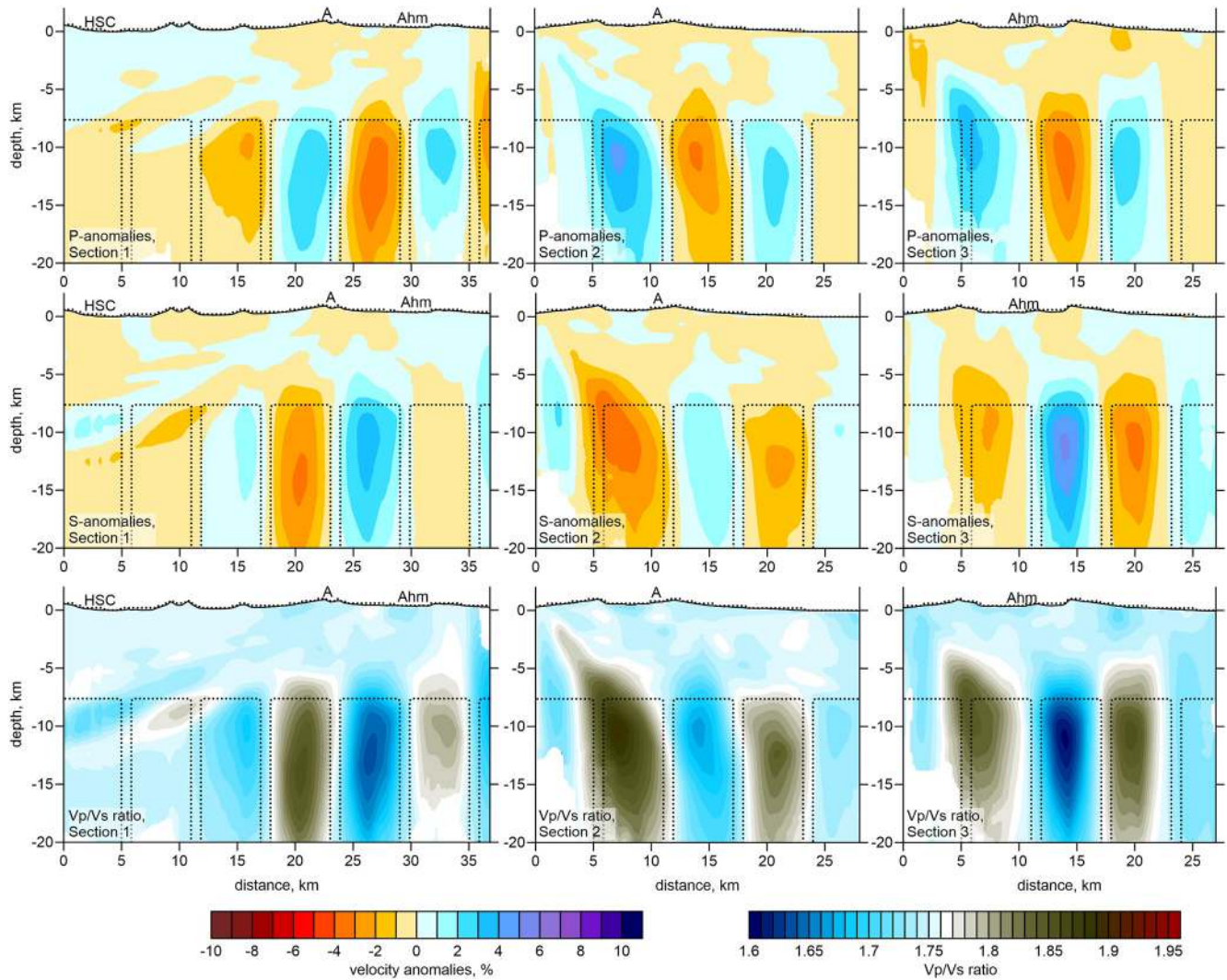
Figure 6. Synthetic tests for checking the resolution in the deeper part of the model. The synthetic models were defined along three vertical sections, same as indicated in Figure 4. The recovery results are presented for the *Vp* and *Vs* anomalies and *Vp/Vs* ratio. The shapes of the synthetic anomalies are highlighted with the dotted lines. Abbreviations: HSC—Hot Spring Cove; A—Cone A; Ahm—Ahmanilix Cone.

the previous test, the anomalies of the *P* and *S* wave velocity had opposite signs. In the resulting images, we can see that we can robustly resolve the upper two layers of anomalies, whereas the third layer below 12 km depth appears not to be recovered.

To further assess the capacity of our algorithm to resolve the deep structures we performed another series of tests presented in Figure 6, in which the anomalies with opposite signs for *dVp* and *dVs* are defined in a single layer located below 8 km depth. We see that most of the anomalies are recovered in the correct locations, which shows that such kinds of structures appear to be trustworthy and there does not appear to be significant smearing of deeper structure to shallower layers.

To further assess the reliability of some structures inferred from the main results and used for interpretation, we have produced a series of tests with realistic anomalies that are presented in Figure 7. In these tests, several patterns are defined along vertical Section 1 by a series of closed polygons, in which we set some values of the *P* and *S* wave velocity anomalies (the values in percent are indicated in Figure 7 by numbers inside each pattern). Here, we consider two models with and without the deep conduit beneath the location of the 2008 eruption (in Figure 7, an anomaly of high *Vp/Vs* ratio at distances of 25–30 km and depths of 10–20 km). In the recovery results (lower row in Figure 7), we can see that in Model 2 (without conduit), there is some downward
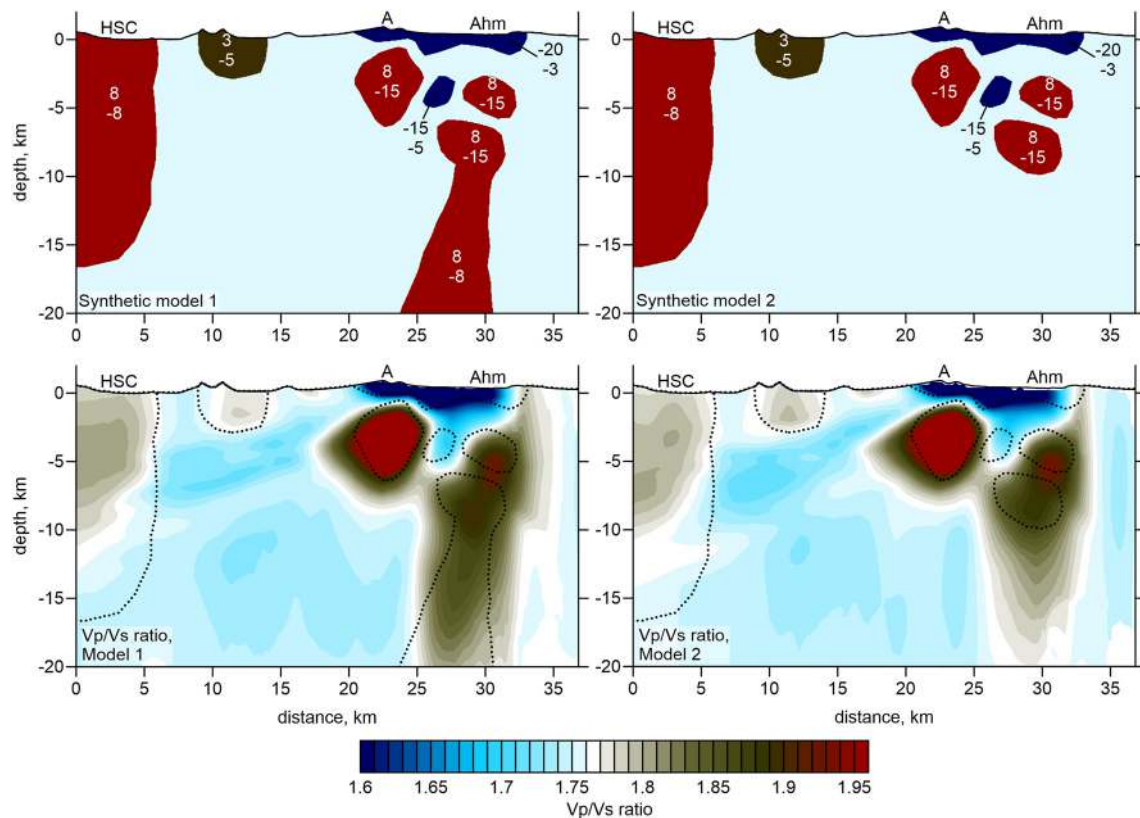
Figure 7. Results of recovery of two synthetic models with realistic shapes of anomalies defined along Section 1 (same as used in Figure 5). The initial synthetic patterns are shown in the upper row; the values of the *P* and *S* wave velocity anomalies are indicated by two numbers inside each pattern. The results of the recovery are shown for the *Vp/Vs* ratio in the lower row. The shapes of the initial anomalies are highlighted with the dotted lines. The comparison of the results of these two tests gives a possibility to assess the reliability of the deep conduit resolving. Abbreviations: HSC—Hot Spring Cove; A—Cone A; Ahm—Ahmanilix Cone.

smearing of the shallower anomalies, which can be misinterpreted as downgoing roots of this structure. However, this case is distinguishable from the result of the recovery of Model 1, in which we defined the deep conduit. These tests demonstrate that we should be prudent when interpreting the structures below 10 km depth. Another structure, which is examined in this test is an anomaly located at the left end of the profile corresponding to the high-seismicity zone beneath the isthmus connecting two parts of the island (in Figure 7, an anomaly of high *Vp/Vs* ratio at distances of 0–5 km and depths of 0–17 km). This area is located outside the network distribution, therefore, the reliability of the derived structures is questionable. In these tests, we defined a large anomaly in a broad range of depths with highly contrasted deviation of the *Vp/Vs* ratio. In the recovery result (lower row in Figure 7), we see that this anomaly is restored with much lower amplitude and at shallower depths. This test shows that we should be careful when considering numerical values of this structure and should only interpret it qualitatively.

It is important that in all tests, we present the distributions of the *Vp/Vs* ratio calculated by the division of the recovered absolute values of *Vp* and *Vs* and show fair recovery of the main structures. These examples show the adequacy of this approach.

The synthetic tests allow also for accessing the accuracy of source parameter determinations. In Figure 8, we present an example of locations of sources in the starting 1D model and in the final 3D velocity distributions in the recovered velocity model and show the errors with respect to their "true" locations. This example corresponds to the case of the synthetic Model 1 with realistic anomalies presented in Figure 7. The black points depict the current hypocenter solutions, whereas the red bars direct to the true source locations. It can be seen that in the starting model, the mean error of source locations is 1.35 km, while in the final model, it is reduced to 1.05 km. The largest errors are observed in the southwestern part of the study area located outside the station network, which remain considerable after completing the iterative inversion procedure. At the same time, for areas inside
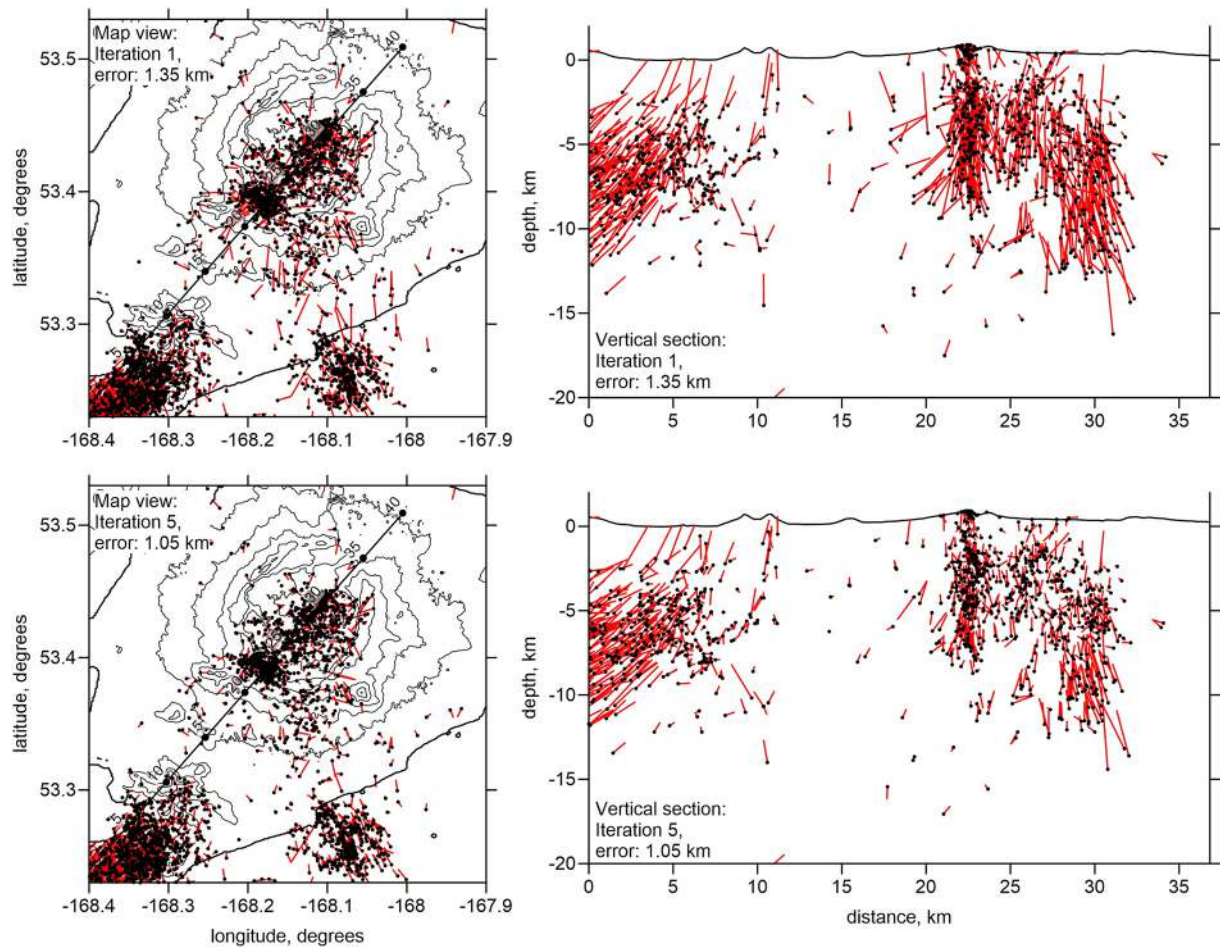
Figure 8. Mislocations of the sources during the synthetic modeling (for the model indicated in the right column in Figure 7) shown in the map view and vertical section. Upper row is the location results with the use of the starting 1D model, and the lower row is the location results in the final 3D velocity model. Black dots indicate the current locations of events, and the red bars direct to the true locations. The mean errors of source locations are indicated in figure captions.

the network, we can visually observe a notable improvement of the source locations during tomography inversions. The similar error range is expected in the case of the experimental data inversion. It should be noted that despite of large location errors for the events located outside the station network, they are useful to obtain a qualitative information about the anomaly located in the left part of the profile in Figure 8. Furthermore, despite of low location accuracy, such out-of-network data provide robust estimates for the relative residuals, which may appear to be important to improve the quality of tomographic inversion (Koulakov, 2009b).

4. Seismic Tomography Results

The main resulting distributions of the anomalies of *Vp* and *Vs*, as well as the *Vp/Vs* ratio are shown in a series of horizontal and vertical sections in Figures 9 and 10. We show the resulting anomalies in horizontal and vertical sections only in areas, where the distance to the nearest node is smaller than a predefined value (2 km in our case). If the distance is larger, we plot it blank. All these results were calculated after five inversion cycles. During the iterative inversion procedure, the *P*-wave residual deviations in the L1 norm were reduced from 0.1455 to 0.1084 s (25.51%), and those of the *S*-wave reduced from 0.1968 to 0.1381 s (29.79%). The detailed interpretation of the resulting models will be presented in the next section. Here we only describe the most important structures obtained from seismic tomography.

As we can see in the horizontal section at zero depth in Figure 9, in the shallowest part of the model, we observe prominent negative anomalies inside the caldera, which likely indicate non-consolidated deposits of volcaniclastic
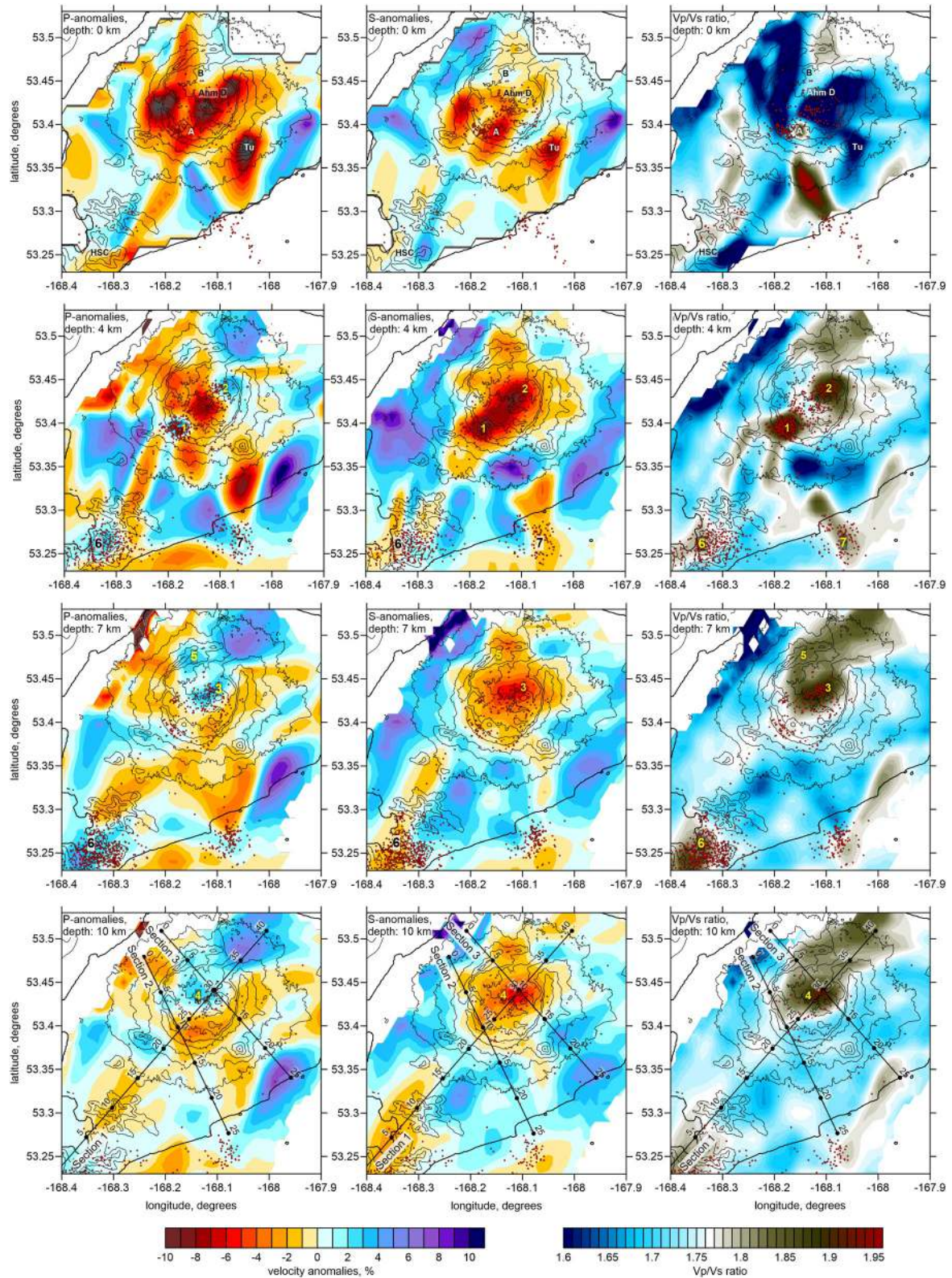
Figure 9. The distributions of the resulting anomalies of *Vp*, *Vs*, and *Vp/Vs* ratio in four horizontal sections. The red dots indicate the locations of seismic events at the vicinity of the corresponding depth levels. The thin black lines shows topography contours with 200 m intervals. The numbers indicate the structures discussed in the text. Indications: A, B and D are the major cones within the caldera; Ahm—Ahmanilix cone; Tu—Mount Tulik; HSC—Hot Spring Cove. The numbers highlight structures discussed in the text.
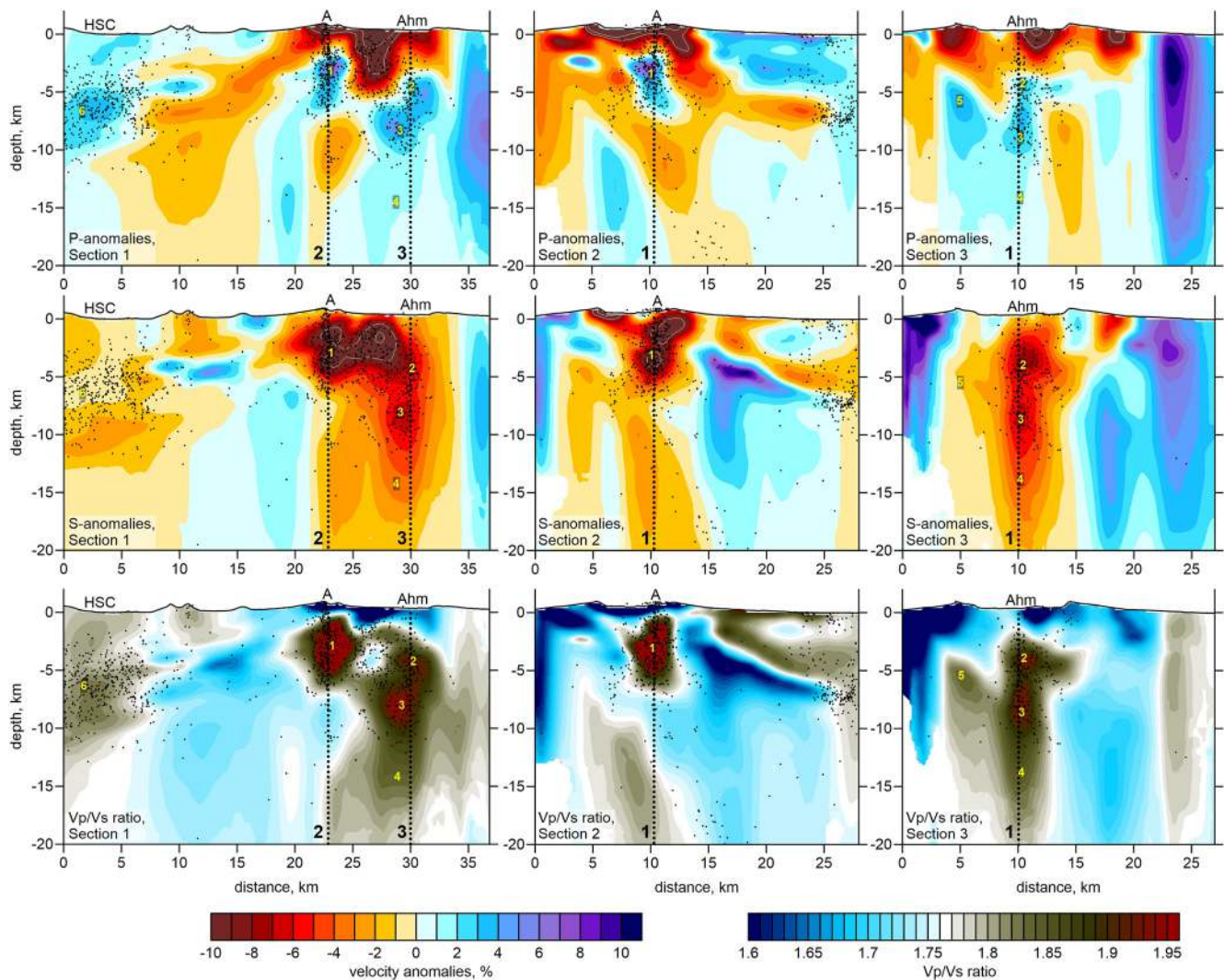
Figure 10. The distributions of the resulting anomalies of *Vp, Vs,* and *Vp/Vs* ratio in three vertical sections with the locations shown in Figure 9. The black dots indicate the projections of seismic events located at distances of less than 2 km from the profile. The numbered dotted lines indicate the intersections with other sections. Abbreviations: HSC—Hot Spring Cove; A—Cone A; Ahm—Ahmanilix Cone.

rocks. The *P*-wave velocity anomalies appear to be stronger than *dVs* and in some places exceed 20%. The stronger *P*-wave anomaly may be indicative of a porous structure of the material, which could behave as a sponge and has low bulk elastic modulus (Takei, 2002). In this case, the *Vp/Vs* shows strongly negative anomaly, which is quite typical for caldera-filling rocks (see, e.g., a similar feature in the Semisopochnoi Island in the tomography model by Yaroshenko et al., 2022). In the vertical section (Figure 10), we can see that this anomaly of low *Vp/Vs* ratio is rather thin and hardly reaches 1 km. As nodes with the minimum spacing of 0.5 km are installed downward starting from the topography surface, the parameterization of our tomography model gives us a possibility to resolve such near-surface structures. At the same time, we should be prudent about assessing qualitative characteristics of such a layer based on one row of nodes. In the shallowest section, the only place within the caldera, where we observe a local anomaly of high *Vp/Vs* ratio, coincides with the cone A in the southeastern part of the caldera, which can be explained by the presence of the magma conduit close to the surface. Another low-velocity anomaly in the uppermost layer is associated with Mt. Tulik, which is a large cinder cone located outside the caldera, having similar mechanical properties as deposits in the caldera.

At the depth of 4 km, the distributions of *dVp, dVs,* and *Vp/Vs* ratio inside the caldera look considerably different compared to the upper section. The low *S*-wave anomaly almost perfectly coincides with the caldera contour, whereas the distribution of the *P*-wave velocity anomalies is more heterogeneous. Below the cones A and D, we

observe locally high *P*-wave velocity patterns (indicated by "1" and "2"), which give the inverse correlation of *dVp* and *dVs* and high values of *Vp/Vs* ratio. Such a relationship is a clear attribute of the presence of the magma with some content of partial melts and fluid saturation (Takei, 2002), which is normally observed in tomography models for most active volcanoes (Bushenkova et al., 2019; Kasatkina et al., 2014; Koulakov et al., 2013).

In the vertical Sections 1 and 2 (Figure 10), we can see that the upper level of the high-*Vp/Vs* anomaly "1" beneath the cone A is located at a depth of less than 500 m, and the bottom side is at ∼5 km b.s.l. The lateral size of this anomaly is approximately 3 km. Beneath the Ahmanilix vent, newly opened during the 2008 eruption, in Sections 1 and 3, we see that the upper limit of the high *Vp/Vs* anomaly "2" is located at the depth of 2 km below surface. The lower limit of this anomaly is not clearly determined in our model: it rather looks as a chain of several structures aligned vertically. The upper anomaly "2" is identified at depths of 2–5 km, and the second one indicated by "3" is located at 6–10 km depth. Below, we observe a vertically oriented anomaly "4", which may represent a deep magma conduit. Based on the two synthetic models with realistic structures presented in Figure 7, despite some obvious vertical smearing in the lower part of our model, we can distinguish such a conduit-related anomaly; though, we should be careful about its numerical parameters.

The results in deeper sections at 7 and 10 km depth look generally similar. The most prominent feature is an anomaly of high *Vp/Vs* ratio indicated by "3" and "4," which is located beneath the caldera and slightly shifted to its northwestern part, where the 2008 eruption occurred. This anomaly, which likely represents a deeper magma reservoir, is also marked by clustered seismicity.

There are two other interesting seismic structures located outside the caldera. As we can see in both horizontal and vertical sections, in the southwest corner of our study area, at the isthmus between two parts of the island, a zone of high seismicity appears to be associated with high *Vp*, low *Vs* and high *Vp/Vs* ratio. In vertical Section 1, this anomaly indicated by "6" is observed down to ∼10 km depth. However, as was shown in the synthetic test with realistic anomalies in Figure 7, in this part of the area, the available data do not enable high-quality recovery, and we can only interpret it qualitatively. In horizontal sections, we see that this zone seems to be connected with the caldera-related anomaly by elongated low-velocity anomalies.

Another zone of elevated seismicity is located in the offshore area, at the southern border of the study area (indicated by "7"). This zone is located outside the station network; therefore we cannot enable sufficient resolution for velocity recovery in this area. However, in the horizontal sections, we see some elongated low-velocity anomalies that may connect this zone with caldera.

We can compare our results with the previous seismic tomography studies of Okmok. Some of the images in the study by Ohlendorf et al. (2014), which were generally based on the same technique and data sources as in this work, appear to be consistent with our results. A prominent low-velocity anomaly of the *P*-velocity inside the caldera determined by them seems to be similar to our results, especially to the anomalies of the *S*-wave velocity. Similar correlation is observed between their distribution of the *P*-wave attenuation and our *S*-wave velocity model. However, in the *S*-wave velocity model, Ohlendorf et al. (2014) revealed a prominent high-velocity anomaly beneath the caldera, which appeared to be inversely correlated with our result. Furthermore, they did not resolve several important features, such as local high *Vp* anomalies at 4 km depth beneath the eruption centers of 1997 and 2008, as apparent in our model, probably because of their larger grid spacing. At the same time, our *S*-wave velocity distribution fairly well correlates with the model by Masterlark et al. (2010) constructed with the use of ambient noise tomography. In that study, the low-velocity anomaly of *Vs* is observed beneath the caldera down to 7 km depth; for the deeper sections, they did not have a sufficient resolution. In the same work, Ohlendorf et al. (2014) estimated the 3D distribution of seismic attenuation. They found low quality factor (or high attenuation) beneath the caldera, which is consistent with the low-velocity anomalies identified in our model.

5. Discussions

Seismic tomography is especially beneficial for identifying the properties of the magma plumbing system beneath active volcanoes, when several seismic attributes, such as *Vp*, Versus and *Vp/Vs* ratio can be determined. Based on the experience of previous seismic tomography studies (Koulakov, 2022; Koulakov et al., 2013, 2020, 2021; Nakajima et al., 2001; Sherburn et al., 2006; Widiyantoro et al., 2018) and the existing experimental results (Takei, 2002), we can single-out several regularities that can be useful to interpret the model obtained in this work. The *P*-wave velocity is primarily sensitive to the composition, whereas the variation of the *S*-wave veloc-
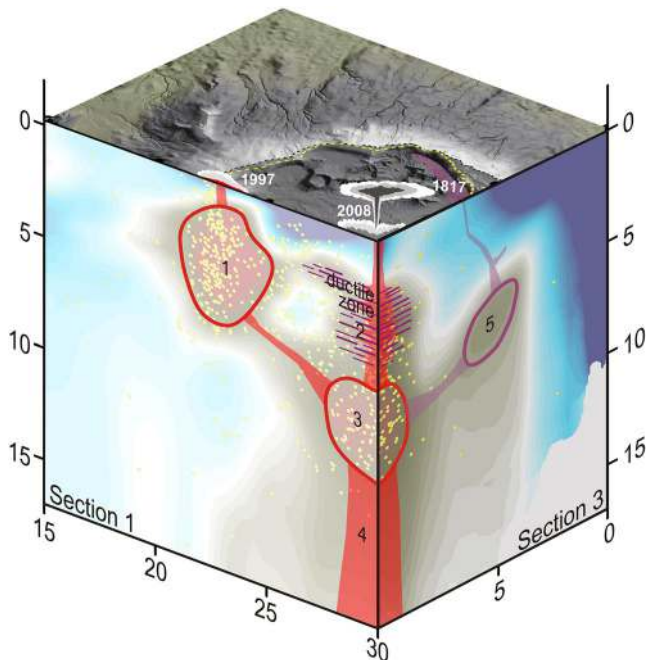
Figure 11. Schematic interpretation of the resulting distributions of the *Vp/Vs* ratio in Sections 1 and 3 in terms of conduits (filled red zones) and magma reservoirs (empty red contours). The yellow dots indicate the seismicity along the sections. On the surface, the detailed topography with the locations of the 1817, 1997, and 2008 eruptions is shown. More details with the description of this figure are in the Discussion section.

ity is mostly controlled by the presence of a liquid phase. The coexistence of higher *P*- and lower *S*-wave velocity, and the corresponding very high values of *Vp/Vs* ratio is a rather typical feature observed beneath many active volcanoes and interpreted as magma reservoirs or conduits (Bushenkova et al., 2019; Koulakov et al., 2013, 2020, 2021). Indeed, the intruded magma has a different composition compared to the host crustal rocks, which determines the higher *Vp*. On the other hand, the active magma sources contain some partial melts and dissolved volatiles that reduce the *S*-wave velocity. This feature provides a very high and contrasted *Vp/Vs* ratio, which is used to determine the geometry of the magma reservoirs and conduits.

It should also be noted that the *P* and *S* wave velocities, when considered separately, in many cases cannot provide unambiguous interpretation. For example, the high *Vp* can be associated with both highly solidified rigid bodies and fresh magma intrusions. The low *S*-wave anomalies can appear to be similar in cases of soft sediments and partially molten magma reservoirs. Thus, when only one of these parameters is available, misinterpretations are possible. The interpretation becomes less ambiguous, when the *Vp* and *Vs* are jointly considered. In particular, the *Vp/Vs* ratio gives clearer images of magma-associated structures, than *Vp* and *Vs* alone and it allows distinguishing the cases mentioned above. For example, considering only *Vs* in Masterlark et al. (2010) does not allow distinguishing between the low-velocity soft rock deposits and underlying magma sources. However, we see that the *Vp/Vs* ratio presented in our study successfully solves this problem and clearly differentiates between the low-*Vp/Vs* in volcanoclastic sediments and the very high *Vp/Vs* ratio in the magma reservoir. Similar differentiation was observed in the area between Avacha and Koryaksky volcanoes (Bushenkova et al., 2019), Akutan (Koulakov et al., 2021) and in many other places. For Okmok, the *Vp/Vs* ratio demonstrates a very shallow location of the magma source beneath the cone A.

Based on the distribution of the *Vp/Vs* ratio in Figures 9 and 10, we can single out several prominent anomalies that might be associated with magma sources. Our schematic interpretation of these structures is presented in Figure 11 Below Cone A, at the intersection of Sections 1 and 2 (Figure 10), we observe a contrasted anomaly "1" with the *Vp/Vs* exceeding 2. According to our model, the upper limit of this anomaly is located at a depth of a few hundred meters and it extends down to ∼6 km. We interpret this anomaly as a magma reservoir that fed the multiple eruptions of Cone A that occurred in the historical times.

Below the cone D and the Ahmanilix vent formed during the 2008 eruption at intersection of Sections 1 and 3 (Figures 10 and 11), we observe a chain of vertically oriented anomalies of high *Vp/Vs* ratio. The deep part indicated by "4" represents a steady magma conduit that is likely responsible for forming Okmok volcano during the entire history of its evolution. Its location roughly corresponds to the summit of the ancestral shield volcano and the conduit is thought to have been active throughout its lifespan.

It appears to be paradoxical that the major recent activity in Okmok occurred along the perimeter of the caldera and not in the center, just above the conduit, where the strongest seismic velocity anomalies are observed. Indeed, most of the historical eruptions, including one in 1997, took place in Cone A, which is laterally shifted to ∼5–7 km from the conduit center. Similar shift is observed for the 1817 eruption that occurred in the cone B in the northern part of the caldera. The Cones F, E, G, H are also located away from the conduit's projection to the surface. The Cones D and Ahmanilix were the only eruption centers, which appeared to be directly connected with the conduit. Similar offsets between magma reservoir and eruptive site exist at other calderas. A notable example is Grimsvotn in Iceland, with a stable magma reservoir at the northern caldera edge, yet the recent eruptions occurred at the southern caldera rim (e.g., Hreinsdottir et al., 2014). In general, Lerner et al. (2020) after analyzing geophysical images on 56 volcanoes found that such a lateral offset of volcanic manifestations with respect to the magma source is rather frequent feature existing in approximately 20% cases, mostly associated

with smaller volcanoes. They found several factors that control such a lateral shifts of active vents, such as age of volcanic systems, composition and magmatic flux.

For the case of Okmok, we explain this paradox by the existence of a mechanical barrier under the central part of the caldera that prevents magma ascending upward and coerces it to find other paths to the periphery of the caldera. The long-term thermal effect from the conduit led to formation of a ductile layer with some content of partial melts. This hypothesis is based on the following arguments. (a) Long-term heating coming from the central conduit should change the rheology of the upper crust from brittle to ductile. (b) Above this area, there are no frequent eruptions; only episodic eruptions with large recurrence time take place there. (c) The magma is enriched with silicic components, which presumes a long time of fractioning and slow ascent of magma sources. (d) Lack of seismicity prior to the 2008 eruption is another argument for ductile rheology. Based on the obtained distribution of the *Vp/Vs* ratio, we propose that this layer corresponds to the anomaly "2" located at depths from 2 to 5 km, perhaps to shallower depths as suggested by the recently proposed very shallow sill-like sources (Xue et al., 2020).

This ductile zone is underlain and likely well connected (Figure 11) to another anomaly of high *Vp/Vs* ratio indicated by "3". Together this shallow system may represent the major magma reservoir feeding the ongoing eruptions at Okmok. This is consistent with the magma source depth estimates obtained from ground deformation modeling, placing magma source regions in the 2–5 km range (e.g., Biggs et al., 2010; Xue et al., 2020). This depth range may indicate that this part of the system is over time active at different depths, or the geodetic data cannot resolve simultaneous activity of both sources unless they are sufficiently separated. This is perhaps due to the limited aperture afforded to geodetic observations by the small radius of the main land mass.

The ductile medium in zone "2" may serve as a barrier for the magma to ascend directly to the surface. Soft rheology does not allow magma to create fractures, and it can only ascend in the form of diapirs due to buoyancy, which enables much slower movement than migration through a brittle medium (e.g., Petford et al., 2000). That is why, to escape from reservoir "3", for magma, it is easier to form some lateral conduits in colder brittle areas where migration can be conducted by hydraulic fracturing. In Figure 11, based on the distribution of the *Vp/Vs* ratio, we identify that such a conduit takes place between the anomalies "3" and "1" that delivers the magmatic material to the reservoir below Cone A. Such a transportation of magma between the reservoirs "3" and "1" likely occurred continuously during the recent epoch, when the regular historical eruptions occurred in Cone A. This has directly provided mafic material to the reservoir "1" from the deep conduit without significant changes at intermediate levels, which is consistent with available information on dominantly basaltic compositions of the eruption products from Cone A (Larsen et al., 2013).

There might be a similar lateral magma conduit toward the anomaly "5" below the northern border of the caldera, which likely represented another magma reservoir that was responsible for the eruption of in 1817. Its upper limit is observed at ~4 km depth. As there is no activity in this part of the caldera for more than 200 years, any traces of shallow conduits bringing magma from the reservoir "5" to the surface were healed, and nowadays they are not visible in the tomography model.

The vertical ascents of magma that caused the formations of cones D and Ahmanilix are rather exceptional cases, which occurred during two time periods since the latest caldera forming eruption of Okmok 2050 years ago. This way of magma ascending is supported by the fact that no increase of seismicity was observed before the 2008 eruption (Larsen et al., 2009, 2015). The seismic activity started only 5 hours prior to the eruption onset, and it likely represented the moment when magma came out from the ductile layer and reached the uppermost brittle cover. In this scenario, the magmas of the 2008 eruption should be contaminated residual magma or crystal mush components existing in zone "2." This is generally consistent with the concept of Larsen et al. (2013) who hypothesized that the 2008 eruption in the northeastern part of the caldera was fed by basaltic magma that initially arrived from a deep reservoir and then was intersected with a more evolved basalt-andesitic magma in shallower layers. This provided a broader range of compositions in different vents of the 2008 eruption compared to those of the 1997 eruption from Cone A.

In the southwestern corner of our study area near the isthmus separating two parts of the Umnak Island, there is an area of high geothermal activity called the Hot Springs Cove. Although it is located outside the seismic station network, a large number of seismic events were recorded in this zone. For seismic tomography, we cannot guarantee high resolution for the structures sitting there. As shown by the synthetic test with realistic anomalies, in this

zone, we can only recover general background velocities. Here, we obtain higher *P* and lower *S* wave velocities (anomaly "6"). In the context of known geothermal activity, it is natural to propose that the low *S*-wave velocity anomalies are associated with high fluid saturation, which can reach significant depths. Based on the existing data, we can speculate that the observed seismicity at depths down to 8–10 km might be caused by upward migration of deep fluids, as the meteoric fluids cannot reach such depths. However, this hypothesis should be verified or disproved by geochemical examination of the hydrothermal sources. The adjacent area of high geothermal activity Geyser Bight was investigated by Nye et al. (1990) with the aim to explore the geothermal resources. In their report, they claimed that hydrothermal activity in this area was mostly driven by circulation of meteoric waters. However the ratio of 3He/4He = 7.4 in emanating gas may provide evidence for a magmatic influence on the hydrothermal system. A similar effect of the deep processes on the hydrothermal processes may take place in the area of Hot Spring Cove. At the same time, we should keep in mind that we are not capable to identify correctly the depth of this anomaly due to a very poor vertical resolution of tomography at the periphery of the model.

It is interesting that in maps of the *P* and *S* wave velocity anomalies at 4 and 7 km, the area of the Hot Springs Cove is connected with the caldera by an elongated low velocity anomaly. As we see in the checkerboard test (Figure 4), the anomalies in this part of the island can be correctly resolved, though with slight diagonal smearing. It can be proposed that this structure represents a hidden tectonic fault that serves as a weakened zone facilitating migration of magma and fluids. Associations of such fault-related linear seismic velocity anomalies with volcanic and geothermal centers is a rather typical feature observed in several volcanic areas, such as Tolbachik in Kamchatka (Koulakov et al., 2017) and Toba Caldera in Sumatra (Koulakov et al., 2016). If there is a tectonic fault, the seismicity beneath this zone can be of tectonic nature. However, an open question remains about lack of seismicity aligned in the fault zone. One explanation could be related to the relatively short observation time, which was not sufficient to record a considerable number of tectonic events. On the other hand, the ruptures might be facilitated by the presence of deeply migrating fluids and therefore they may provide displacements of crustal blocks without earthquakes.

6. Conclusions

Here, we revisit the local earthquake data for Okmok volcano provided by the Alaska Volcano Observatory to build a new seismic tomography model. Owing to implementing the LOTOS tomography algorithm with adaptive parameterization and using a larger data set compared to the previous study by Ohlendorf et al. (2014), we have obtained higher resolution for the resulting distributions of the *P* and *S* wave velocities and the *Vp/Vs* ratio. In the derived models we can identify some important features that were not seen before and that provide important insight on the geometry of magma sources beneath Okmok. A number of synthetic tests have demonstrated the resolution limitations for the recovered models and proven the reliability of the main structures used for the interpretation. To reveal the geometry of the magma sources, we mostly use the distribution of the *Vp/Vs* ratio, which appears to be a sensitive attribute for the presence of magma having different composition and containing partial melts and dissolved fluids.

Based on the retrieved seismic model, we conclude that the steady magma conduit, which is responsible for forming the entire Okmok volcanic complex, is located beneath the northeastern part of the caldera. At depths of 6–10 km, this conduit is headed by the main reservoir, which is thought to be the main magma source for all volcanic vents along the inner perimeter of the Okmok caldera.

We speculate that for the magma from the deep conduit, it is difficult to ascend vertically because of the presence of a ductile layer at the depth of 2–5 km that serves as a natural barrier for ascending magma. In the post-caldera time, only in two cases, magma could pass this layer and reach the surface. In the first case, it caused the formation of Cone D relatively soon after the Okmok II caldera forming eruption occurred. The second eruption occurred in 2008 and resulted in the formation of the new cone Ahmanilix. In this sense, the vertical transport of magma directly from the deep conduit appears to be exceptional for Okmok.

In most cases, magma escapes from the central reservoirs toward the periphery of the caldera and creates local reservoirs beneath active vents. In historical times, the most active vent, where the majority of the recorded eruptions of Okmok occurred, corresponds to the cone A in the southwestern part of caldera. Below this location, we observe a large anomaly with the upper boundary located at the depth of a few hundred meters and the bottom at

~5 km depth, which represents the magma reservoir that feeds all these eruptions. In our tomography model, we see that this anomaly is connected with the central magma reservoir, which provides for continuous infill of the storage below the cone A by fresh magma with mafic composition. Another periphery reservoir and a conduit can be detected below Cone B, which was the main vent active during the 1817 eruption; however, it appears to be less clear, as it might have been dissipated during more than 200 years of quiescence.

Our result shows that the magma reservoir beneath the cone A is located very close to the surface, possibly at a few hundred meters depth. This finding should be further verified using alternative geophysical methods, such as active seismics or electromagnetic methods. In case it is confirmed, this would give a unique possibility to reach the magma storage by a relatively small borehole and investigate it for the purposes of using the heat of active magma to produce geothermal energy.

Data Availability Statement

Derived products from this publication, including travel times of *P* and *S* waves and the full folder of the LOTOS code that allows reproducing all the results of this research are presented in the file repository: Kasatkina and Koulakov (2022). Data and program codes to reproduce the results of seismic tomography for Okmok [Dataset]. Zenodo. https://doi.org/10.5281/zenodo.6475984.

References

Biggs, J., Lu, Z., Fournier, T., & Freymueller, J. T. (2010). Magma flux at Okmok volcano, Alaska, from a joint inversion of continuous GPS, campaign GPS, and interferometric synthetic aperture radar. *Journal of Geophysical Research*, *115*(B12). https://doi.org/10.1029/2010JB007577

Bingham, D. K., & Stone, D. B. (1972). Palaeosecular variation of the geomagnetic field in the Aleutian islands, Alaska. *Geophysical Journal of the Royal Astronomical Society*, *28*, 317–335. https://doi.org/10.1111/j.1365-246x.1972.tb06796.x

Burgisser, A. (2005). Physical volcanology of the 2,050 bp caldera-forming eruption of Okmok volcano, Alaska. *Bulletin of Volcanology*, *67*, 497–525. https://doi.org/10.1007/s00445-004-0391-5

Bushenkova, N., Koulakov, I., Senyukov, S., Gordeev, E. I., Huang, H.-H., El-Khrepy, S., & Al-Arifi, N. (2019). Tomographic images of magma chambers beneath the Avacha and Koryaksky volcanoes in Kamchatka. *Journal of Geophysical Research: Solid Earth*, *124*, 9694–9713. https://doi.org/10.1029/2019JB017952

Byers, F. M., Jr. (1959). Geology of Umnak and Bogoslof islands, Aleutian island, Alaska. *US Geological Survey Bulletin*, *1028-L*, 107–367.

Dixon, J. P., Cameron, C. E., Iezzi, A. M., & Wallace, K. (2017). 2015 volcanic activity in Alaska-summary of events and response of the Alaska Volcano Observatory. *U.S. Geological Survey Scientific Investigations Report*, 2017-5104, *61*. https://doi.org/10.3133/sir20175104

Fournier, T., Freymueller, J., & Cervelli, P. (2009). Tracking magma volume recovery at Okmok volcano using GPS and an unscented Kalman filter. *Journal of Geophysical Research*, *114*, B02405. https://doi.org/10.1029/2008JB005837

Freymueller, J. T., Kaufman, A. M., & Kaufman, A. M. (2010). Changes in the magma system during the 2008 eruption of Okmok volcano, Alaska, based on GPS measurements. *Journal of Geophysical Research*, *115*(B12), 115–132. https://doi.org/10.1016/j.jvolgeores.2012.04.021

Haney, M. M. (2010). Location and mechanism of very long period tremor during the 2008 eruption of Okmok volcano from interstation arrival times. *Journal of Geophysical Research*, *115*, 13. https://doi.org/10.1029/2010JB007440

Hreinsdóttir, S., Sigmundsson, F., Roberts, M. J., Björnsson, H., Grapenthin, R., Arason, P., et al. (2014). Volcanic plume height correlated with magma-pressure change at Grímsvötn volcano, Iceland. *Nature Geoscience*, *7*(3), 214–218.

Johnson, J. H., Prejean, S., Savage, M. K., & Townend, J. (2010). Anisotropy, repeating earthquakes, and seismicity associated with the 2008 eruption of Okmok volcano, Alaska. *Journal of Geophysical Research*, *115*, B00B04. https://doi.org/10.1029/2009JB006991

Kasatkina, E., & Koulakov, I. (2022). Data and program codes to reproduce the results of seismic tomography for Okmok. https://doi.org/10.5281/zenodo.6475984

Kasatkina, E., Koulakov, I., West, M., & Izbekov, P. (2014). Seismic structure changes beneath Redoubt volcano during the 2009 eruption inferred from local earthquake tomography. *Journal of Geophysical Research: Solid Earth*, *119*, 4938–4954. https://doi.org/10.1002/2013JB010935

Koulakov, I. (2009a). LOTOS code for local earthquake tomographic inversion: Benchmarks for testing tomographic algorithms. *Bulletin of the Seismological Society of America*, *99*, 194–214. https://doi.org/10.1785/0120080013

Koulakov, I. (2009b). Out-of-network events can be of great importance for improving results of local earthquake tomography. *Bulletin of the Seismological Society of America*, *99*(4), 2556–2563. https://doi.org/10.1785/0120080365

Koulakov, I., Abkadyrov, I., Al Arifi, N., Deev, E., Droznina, S., Gordeev, E. I., et al. (2017). Three different types of plumbing system beneath the neighboring active volcanoes of Tolbachik, Bezymianny, and Klyuchevskoy in Kamchatka. *Journal of Geophysical Research: Solid Earth*, *122*, 3852–3874. https://doi.org/10.1002/2017JB014082

Koulakov, I., Boychenko, E., & Smirnov, S. Z. (2020). Magma chambers and meteoric fluid flows beneath the Atka volcanic complex (Aleutian Islands) inferred from local earthquake tomography. *Geosciences*, *10*, 214. https://doi.org/10.3390/geosciences10060214

Koulakov, I., Kasatkina, E., Shapiro, N. M., Jaupart, C., Vasilevsky, A., El-Khrepy, S., et al. (2016). The feeder system of the Toba supervolcano from the slab to the shallow reservoir. *Nature Communications*, *7*, 12228. https://doi.org/10.5194/se-7-965-2016

Koulakov, I., Komzeleva, V., Smirnov, S. Z., & Bortnikova, S. B. (2021). Magma-fluid interactions beneath Akutan volcano in the Aleutian arc based on the results of local earthquake tomography. *Journal of Geophysical Research: Solid Earth*, *126*(1), e2020JB021192. https://doi.org/10.1029/2020JB021192

Koulakov, I., West, M., & Izbekov, P. (2013). Fluid ascent during the 2004–2005 unrest at Mt. Spurr inferred from seismic tomography. *Geophysical Research Letters*, *40*(17), 4579–4582. https://doi.org/10.1002/grl.50674

Koulakov, I. Yu. (2022). Seismic tomography of Kamchatkan volcanoes. *Russian Geology and Geophysics*. https://doi.org/10.2113/RGG20214380

Larsen, J. F., Neal, C., Schaefer, J., Beget, J., & Nye, C. (2007). Late pleistocene and holocene caldera-forming eruptions of Okmok caldera, Aleutian islands, Alaska. *American Geophysical Union Geophysical Monograph Series*, *172*, 343–364. https://doi.org/10.1029/172GM24

Larsen, J. F., Neal, C., Webley, P., Freymueller, J., Haney, M., McNutt, S., & Wessels, R. (2009). Eruption of Alaska volcano breaks historic pattern. *Eos: Transactions – American Geophysical Union*, *90*(20), 173–174. https://doi.org/10.1029/2009eo200001

Larsen, J. F., Schaefer, C. A., Kaufman, J. R., & Lu, Z. (2015). The 2008 phreatomagmatic eruption of Okmok volcano, Aleutian islands, Alaska: Chronology, deposits, and landform changes. *Bulletin of Volcanology*, *77*(69). https://doi.org/10.1007/s00445-015-0952-9

Larsen, J. F., Śliwiński, M. G., Nye, C., Cameron, C., & Schaefer, J. R. (2013). The 2008 eruption of Okmok volcano, Alaska: Petrological and geochemical constraints on the subsurface magma plumbing system. *Journal of Volcanology and Geothermal Research*, *264*, 85–106. https://doi.org/10.1016/j.jvolgeores.2013.07.003

Lerner, A. H., O'Hara, D., Karlstrom, L., Ebmeier, S. K., Anderson, K. R., & Hurwitz, S. (2020). The prevalence and significance of offset magma reservoirs at arc volcanoes. *Geophysical Research Letters*, *47*(14), e2020GL087856.

Lu, Z., & Dzurisin, D. (2014). InSAR imaging of Aleutian volcanoes. In *InSAR imaging of aleutian olcanoes* (pp. 87–345). Springer Berlin Heidelberg. https://doi.org/10.1007/978-3-642-00348-6_6

Lu, Z., Mann, D., Freymueller, J. T., & Meyer, D. J. (2000). Synthetic aperture radar interferometry of Okmok volcano, Alaska: Radar observations. *Journal of Geophysical Research*, *105*, 10791–10806. https://doi.org/10.1029/2000JB900034

Mann, D., Freymueller, J., & Lu, Z. (2002). Deformation associated with the 1997 eruption of Okmok volcano, Alaska. *Journal of Geophysical Research*, *107*(B4), 2072. https://doi.org/10.1029/2001JB000163

Masterlark, T., Feigl, K. L., Haney, M., Stone, J., Thurber, C., & Ronchin, E. (2012). Nonlinear estimation of geometric parameters in FEMs of volcano deformation: Integrating tomography models and geodetic data for Okmok volcano, Alaska. *Journal of Geophysical Research*, *117*, B02407. https://doi.org/10.1029/2011JB008811

Masterlark, T., Haney, M., Dickinson, H., Fournier, T., & Searcy, C. (2010). Rheologic and structural controls on the deformation of Okmok volcano, Alaska: FEMs, InSAR, and ambient noise tomography. *Journal of Geophysical Research*, *115*(B2), B02409. https://doi.org/10.1029/2009JB006324

McConnell, J. R., Sigl, M., Plunkett, G., Burke, A., Kim, W. M., Raible, C. C., et al. (2020). Extreme climate after massive eruption of Alaska's Okmok volcano in 43 BCE and effects on the late roman republic and ptolemaic kingdom. *Proceedings of the National Academy of Sciences*, *117*(27), 15443–15449. https://doi.org/10.1073/pnas.2002722117

Miller, T. P., McGimsey, R. G., Richter, D. H., Riehle, J. R., Nye, C. J., Yount, M. E., & Dumoulin, J. A. (1998). Catalog of the historically active volcanoes of Alaska. *Department of the Interior, U.S. Geological Survey*, 98–582. https://doi.org/10.3133/ofr98582

Nakajima, J., Matsuzawa, T., Hasegawa, A., & Zhao, D. (2001). Three-dimensional structure of *Vp*, *Vs*, and *Vp/Vs* beneath northeastern Japan: Implications for arc magmatism and fluids. *Journal of Geophysical Research*, *106*(B10), 21843–21857. https://doi.org/10.1029/2000jb000008

Nolet, G. (1987). Seismic wave propagation and seismic tomography. *Seismic Tomography*, 1–23. https://doi.org/10.1007/978-94-009-3899-1_1

Nye, C. J., Motyka, R. J., Turner, D. L., & Liss, S. A. (1990). *Geology and geochemistry of the geyser bight geothermal area, Umnak island, Aleutian islands, Alaska. Fairbanks, AK*. Graphic North Printing, Division of Geological and Geophysical Surveys.

Ohlendorf, S. J., Thurber, C. H., Pesicek, J. D., & Prejean, S. G. (2014). Seismicity and seismic structure at Okmok volcano, Alaska. *Journal of Volcanology and Geothermal Research*, *278*, 103–119. https://doi.org/10.1016/j.jvolgeores.2014.04.002

Paige, C. C., & Saunders, M. A. (1982). LSQR: An algorithm for sparse linear equations and sparse least squares. *ACM Transactions on Mathematical Software*, *8*(1), 43–71. https://doi.org/10.1145/355984.355989

Pesicek, J. D., Sileny, J., Prejean, S. G., & Thurber, C. H. (2012). Determination and uncertainty of moment tensors for microearthquakes at Okmok volcano, Alaska. *Geophysical Journal International*, *190*(3), 1689–1709. https://doi.org/10.1111/j.1365-246X.2012.05574.x

Petford, N., Cruden, A. R., McCaffrey, K. J. W., & Vigneresse, J.-L. (2000). Granite magma formation, transport and emplacement in the Earth's crust. *Nature*, *408*, 669–673. https://doi.org/10.1038/35047000

Qu, F., Lu, Z., Poland, M., Freymueller, J., Zhang, Q., & Jung, H. S. (2015). Post-eruptive inflation of Okmok volcano, Alaska, from InSAR, 2008–2014. *Remote Sensing*, *7*(12), 16778–16794. https://doi.org/10.3390/rs71215839

Ryan, W. B. F., Carbotte, S. M., Coplan, J. O., O'Hara, S., Melkonian, A., Arko, R., et al. (2009). Global multi-resolution topography synthesis. *Geochemistry, Geophysics, Geosystems*, *10*, Q03014. https://doi.org/10.1029/2008GC002332

Schaefer, J. R., Larsen, J. F., & Unema, J. A. (2012). *Digital elevation model (DEM) and shaded relief image of Okmok caldera, 2010*. Alaska Division of Geological & Geophysical Surveys. Raw Data File 2011-6. https://doi.org/10.14509/23223

Sherburn, S., White, R. S., & Chadwick, M. (2006). Three-dimensional tomographic imaging of the Taranaki volcanoes, New Zealand. *Geophysical Journal International*, *166*(2), 957–969. https://doi.org/10.1111/j.1365-246x.2006.03040.x

Takei, Y. (2002). Effect of pore geometry on V_P/V_S: From equilibrium geometry to crack. *Journal of Geophysical Research*, *107*, 2043. https://doi.org/10.1029/2001JB000522

Um, J., & Thurber, C. H. (1987). A fast algorithm for two-point seismic ray tracing. *Bulletin of the Seismological Society of America*, *77*, 972–986. https://doi.org/10.1785/bssa0770030972

Walwer, D., Ghil, M., & Calais, E. (2019). Oscillatory nature of the Okmok volcano's deformation. *Earth and Planetary Science Letters*, *506*, 76–86. https://doi.org/10.1016/j.epsl.2018.10.033

Widiyantoro, S., Ramdhan, M., Métaxian, J. P., Cummins, P. R., Martel, C., Erdmann, S., et al. (2018). Seismic imaging and petrology explain highly explosive eruptions of Merapi volcano, Indonesia. *Scientific Reports*, *8*(1), 1–7. https://doi.org/10.1038/s41598-018-31293-w

Xue, X., Freymueller, J., & Lu, Z. (2020). Modeling the posteruptive deformation at Okmok based on the GPS and InSAR time series: Changes in the shallow magma storage system. *Journal of Geophysical Research: Solid Earth*, *125*, e2019JB017801. https://doi.org/10.1029/2019JB017801

Yaroshenko, G., Koulakov, I., Al-Arifi, N., Qaysi, S., & El-Khrepy, S. (2022). Structure of the magma plumbing system beneath semisopochnoi island (Aleutian arc) inferred from seismic tomography. *Scientific Reports*, *12*, 10771. https://doi.org/10.1038/s41598-022-14794-7